Astronomy & Astrophysics

LETTER TO THE EDITOR

Returning magnetic flux in sunspot penumbrae

B. Ruiz Cobo[1] and A. Asensio Ramos[2]

[1] Instituto de Astrofísica de Canarias, 38205 La Laguna, Tenerife, Spain
 e-mail: brc@iac.es
[2] Departamento de Astrofísica, Universidad de La Laguna, 38205 La Laguna, Tenerife, Spain

ABSTRACT

Aims. We study the presence of reversed polarity magnetic flux in sunspot penumbra.
Methods. We applied a new regularized method to deconvolve spectropolarimetric data observed with the spectropolarimeter SP onboard Hinode. The new regularization is based on a principal component decomposition of the Stokes profiles. The resulting Stokes profiles were inverted to infer the magnetic field vector using SIR.
Results. We find, for the first time, reversed polarity fields at the border of many bright penumbral filaments in the whole penumbra.

Key words. methods: observational – methods: numerical – Sun: magnetic topology – sunspots – techniques: polarimetric

1. Introduction

Magnetohydrodynamic simulations of sunspots (Rempel et al. 2009a,b; Rempel 2012) have successfully reproduced many aspects of sunspot penumbrae as produced by magneto-convection in inclined magnetic fields. As a consequence, magnetic field with inverse polarity and downflow velocities should be observed all along the boundaries of bright penumbral filaments. While observational evidence for convective downflows in the whole penumbra has been recently reported (Scharmer et al. 2011; Scharmer & Henriques 2012; Joshi et al. 2011), the reversed flux has only been observed in the outer penumbra (Westendorp Plaza et al. 1997, 2001; del Toro Iniesta et al. 2001). But even with the highest spatial resolution spectropolarimetry, we have been unable to observe them in the inner penumbra (Langhans et al. 2005). When inverting data from the Advanced Stokes Polarimeter (Elmore 1992) under the micro-structured magnetic atmosphere (MISMA) hypothesis, Sánchez Almeida (2005) found that penumbral filaments could be interpreted as bundles of magnetic field lines ranging over all inclination angles. In his Ph.D. thesis, Franz (2011) shows how the opposite polarity fields in penumbral filaments are responsible for a weak third lobe in Stokes *V* that appears on the red wing of 40% of the penumbral spectra of the two iron lines at 630 nm observed with the Hinode spectropolarimeter (Hinode/SP, Lites et al. 2001; Kosugi et al. 2007). For recent reviews see Borrero & Ichimoto (2011), Bellot Rubio (2010), Borrero (2009), Schlichenmaier (2009), or Tritschler (2009).

2. Observations

The active region NOAA 10953 was mapped at an average heliocentric angle of $\theta = 12.8°$ using Hinode/SP on 2007 Apr. 30, between 18:35 and 22:30 UT. This active region has recently been analyzed by Ichimoto (2010) and Louis et al. (2009, 2011). The region was scanned in ~1000 steps, with a step width of $0\farcs148$ and a slit width of $0\farcs158$, recording the full Stokes vector of the pair of the neutral iron lines at 630 nm with a spectral sampling of 21.46 mÅ. The spatial resolution was ~$0\farcs32$. The integration time was 4.8 s, resulting in an approximate noise level of 1.2×10^{-3}. To calibrate the spectra, we averaged the intensity profiles coming from a $5'' \times 5''$ region of quiet Sun near the disk center. We compared this average profile to the Fourier transform spectrometer spectral atlas (Kurucz et al. 1984; Brault & Neckel 1987) once it was convolved with the spectral point spread function (PSF) of Hinode. We have found that a veil of 3.4% must be subtracted from the continuum intensity before normalization. This value is similar to the stray-light contaminations of 4.7% found by Danilovic et al. (2008) and 5% found by Socas-Navarro (2011). The wavelength was calibrated by assuming that the average umbral profile is at rest.

3. Deconvolution

Deconvolving two-dimensional spectropolarimetric data wavelength by wavelength has some drawbacks. First, the number of deconvolutions one has to carry out is large. Second, many of these wavelengths contain practically no relevant information in Stokes *Q*, *U* and *V*, apart from the noise. This potentially leads to an enhancement of the noise level unless it is filtered. For this reason, and in order to overcome these two problems, we introduced a regularization into the deconvolution (the details will be given in Asensio Ramos et al. in prep). This regularization acts on the spectral dimension of the data by assuming that the original Stokes profiles (before reaching the telescope) at each pixel can be written as a truncated linear combination of the principal components $\{\phi_i(\lambda)\}$ obtained from the observations, so that

$$\mathbf{O}(\lambda) = \sum_{i=1}^{N} \omega_i \phi_i(\lambda), \tag{1}$$

where N is the number of eigenfunctions needed to reproduce the profiles to adequate precision. Under this assumption, and assuming that the monochromatic PSF is independent of wavelength, the observed Stokes profiles is given by

$$\mathbf{I}(\lambda) = \sum_{i=1}^{N} (\omega_i * \mathbf{P}) \phi_i(\lambda) + \mathbf{N}, \tag{2}$$

where $\mathbf{P}$ is the PSF (kindly provided by van Noort[1]), and $\mathbf{N}$ is a Gaussian noise component with zero mean and variance σ^2.

---

[1] Described in van Noort (2012) and obtained from the Hinode pupil specified by Suematsu et al. (2008).
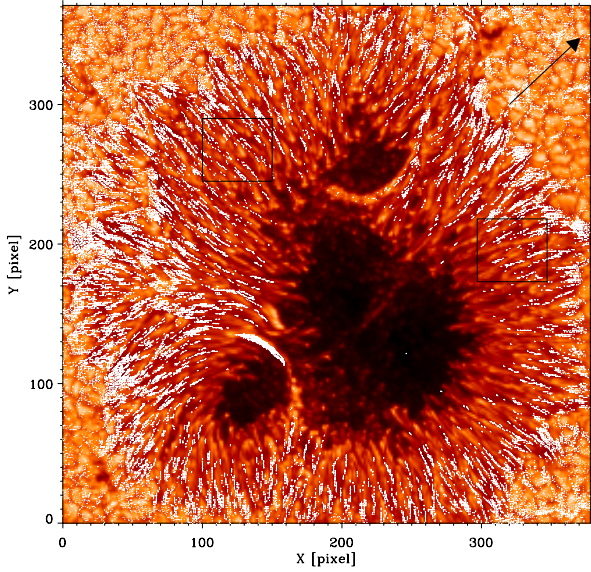
Fig. 1. Deconvolved continuum intensity. White arrows correspond to the horizontal component of the magnetic field in points with reversed polarity. Black rectangles mark the areas area amplified in Fig. 3. The black arrow points to the disk center.
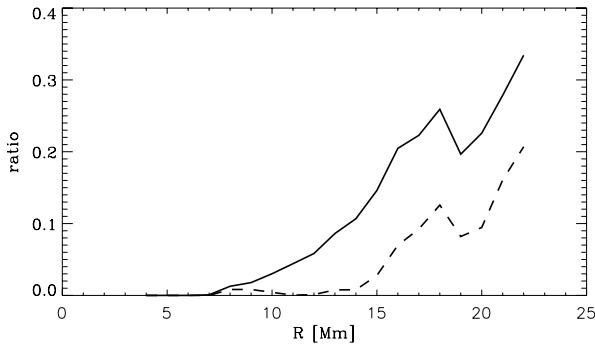

Fig. 2. Filling factors of regions with reversed polarity at $\tau = 0.1$ after (solid line) and before (dashed line) deconvolution.

Given the orthonormality of the principal components, the projection images ω_i fulfill:

$$\langle \mathbf{I}(\lambda), \phi_k(\lambda) \rangle = \omega_k * \mathbf{P} + \mathbf{N} \tag{3}$$

where the noise is still Gaussian with zero mean and variance σ^2. Consequently, the regularization process we have used implies that we have to deconvolve the projections of the original measured data onto the basis functions $\phi_k(\lambda)$ and reconstruct the unperturbed image using Eq. (1). One of the most interesting properties of this approach is that, since the real signal in each pixel only appears in the first few coefficients (a fundamental consequence of the principal component decomposition), the influence of noise is largely minimized. We deconvolve these images using a Richardson-Lucy algorithm (Richardson 1972; Lucy 1974) controlling the number of iterations to avoid any ringing effect (although we hardly see any fringing given the absence of noise in the projection images).

4. Inversion

The Stokes inversion based on response functions (SIR) code (Ruiz Cobo & del Toro Iniesta 1992) was applied on the deconvolved spectra to derive the stratification of temperature T,
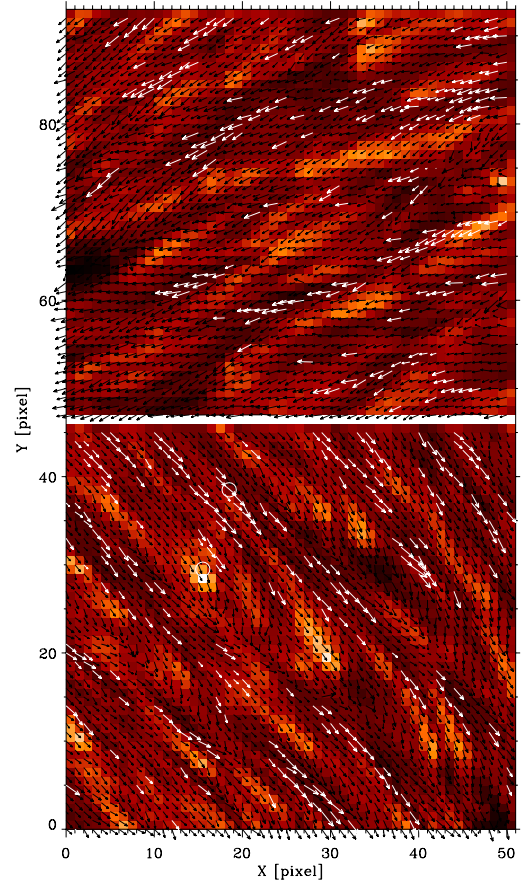
Fig. 3. Sections in the center side (*upper*) and limb side (*bottom*) penumbra White arrows correspond to the horizontal component of the magnetic field in points with reversed polarity. White circles at (15,29) and (18,38) mark the position of the spectra shown in Fig. 4.

magnetic field strength B, inclination γ, azimuth ϕ, and line of sight velocity V_{los} versus continuum optical depth τ. The values of those parameters were retrieved at a number of optical depth points called nodes. We used a maximum of seven nodes in T, five in B, V_{los}, γ, and two in ϕ. Five different initializations were used to avoid local minima. Because we are interested in the penumbra and our sunspot has negative polarity, we solved the 180° ambiguity of the azimuth by choosing the value in such a way that the magnetic field vector $\boldsymbol{B}$ points to the umbra. Additionally, we transformed $\boldsymbol{B}$ into the local reference frame. Likewise, we applied the same inversion procedure to the original data, i.e., before the deconvolution from the spatial PSF.

5. Results and discussion

In Fig. 1 we present the reconstructed continuum intensity map of the region containing the sunspot, including the horizontal component of the magnetic filed vector in those pixels in which the field presents a reversed polarity. We note how the pixels showing reversed polarity are distributed over the whole penumbra, with the exception of the most inner part. There is an obvious concentration of reversed flux in some patches of the most external part of the outer penumbra. The full spot has a total unsigned magnetic flux of $\Phi_z = 1.19 \times 10^{22}$ Mx, measured at $\tau = 0.1$, while the flux of the penumbra is $\Phi_z = 0.79 \times 10^{22}$ Mx. The reversed flux in the penumbra accounts for 8.4% of this penumbral flux, amounting to 17% of the pixels of the penumbra, and 72% of these pixels present a positive
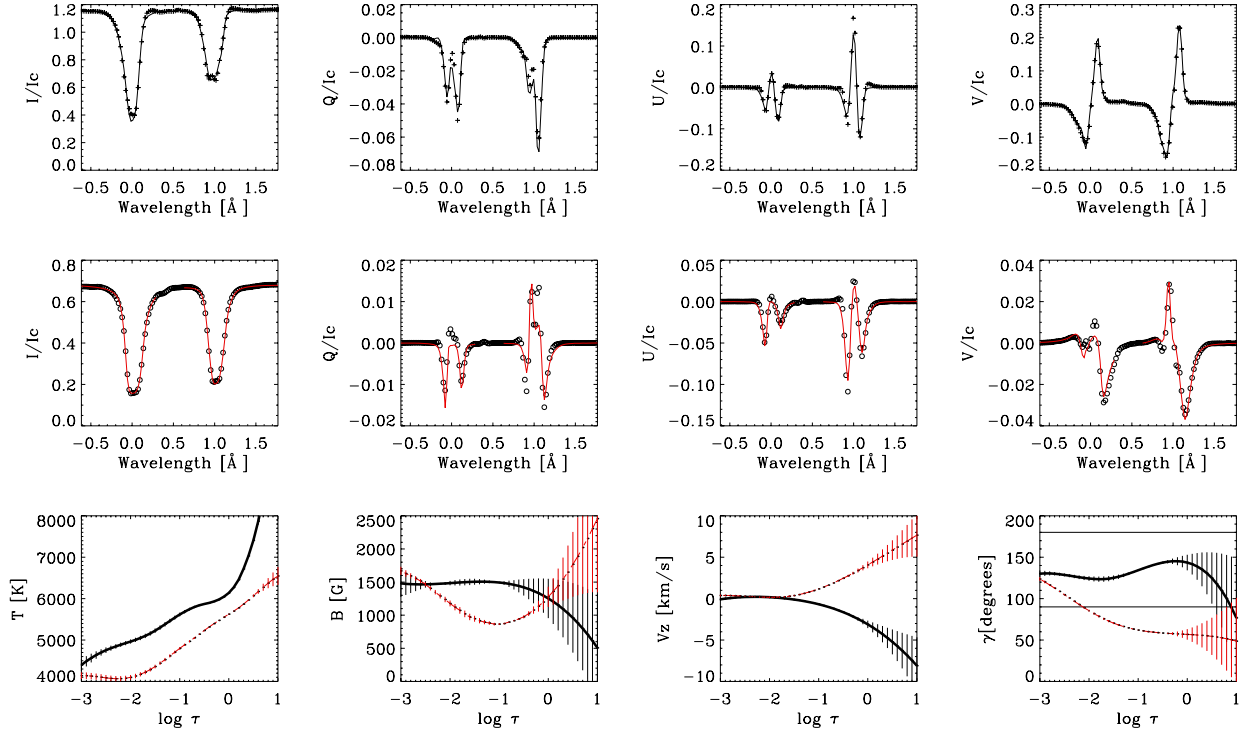
Fig. 4. *Upper 4 panels*: stokes profiles and best fits obtained by the SIR inversion applied to a pixel in a penumbral filament harboring a magnetic field with the same polarity of the umbra. *Middle 4 panels*: the same for a pixel with the reversed polarity. *Lower 4 panels*: corresponding atmospheric models. The thick black line corresponds to the profiles shown in the *upper row* of this figure and the red ones to the *middle row*.

velocity (downflow). This figure should be compared with the 56% of the pixels of the full penumbra harboring downflows. The correlation between downflows and reversed fields is probably tighter than this 72% because the velocities are measured in the line of sight reference frame, while **B** has been translated into the local reference frame. The preceding figures increase to 30% (reversed flux over total unsigned flux), with 28% of the pixels harboring reversed polarity and 88% of these presenting downflows at $\tau = 1$. Nevertheless, **B** at $\tau = 1$ has a large uncertainty (usually error bars around 600 G in *B* and 15° in γ).

In Fig. 2 we plot the ratio of pixels harboring inverse polarity with respect to the total number of pixels at $\tau = 0.1$ versus the radius from the center of the umbra, after and before deconvolution. The ratios shown in this figure are very similar to those found in numerical simulations (cf. Fig. 13 in Rempel 2012), except for the increase in the filling factor at radii larger than 19 Mm. We need to take into account that our sunspot is not circular and that the upper left penumbra is certainly wider that the bottom right one. However, the similitude with the numerical simulation results is clear, even considering the difference in spatial resolution. Also the inverse polarity pixels for the original data (before deconvolution) only appear at a radius larger than 14 Mm, while after deconvolution we already found inverse polarity pixels at 8 Mm.

In Fig. 3 we show a zoom of two middle penumbra regions (marked with black rectangles in Fig. 1), one on the limb side (bottom panel) and the other on the center side (upper panel). It is conspicuous that the reversed field pixels are in dark filaments and, in many cases, they seem to mainly be placed at the boundary of bright filaments. The circles at (15,29) and (18,38) mark the position of the pixels whose spectra are shown in Fig. 4. The first one is an example of a normal polarity pixel, and the second is a reversed one. The corresponding stratification of T, B, V_z, and γ in a local reference frame is plotted in panels in the bottom row. This pixel harbors an upflow and a negative

polarity ($\gamma > 90°$). The example of a reversed polarity pixel is plotted in the middle row. The corresponding stratification through the photosphere is plotted in the panels in the bottom row. The Stokes *V* profiles present a clear positive polarity (opposite to that of the umbra). Also we note the small amplitude of these Stokes *V* profiles. The corresponding model is considerably cooler, and it presents a downflow and a weaker field with a inclination lower than 90° at all layers below optical depth 0.01. These profiles are contaminated by a small residual of the normal polarity profile. There is a small reversed lobe at the blue wing of the Stokes *V* profiles of both 630.1 nm and 630.2 nm Fe I lines. This small contamination and the consequent asymmetry of the Stokes profiles could be responsible for the strong gradient of both *B* and γ, although the profiles are not perfectly reproduced by the model.

It is well known that any overcorrection of stray light in a spectral image generates inverse polarity profiles at the border of bright structures. This is caused because a deconvolution is equivalent, in those pixels, to the substraction of a fraction of the spectral profile of the brighter neighbors. We can assess that our inverse profiles do not come from such an artificial effect for two reasons. First, we have undercorrected our data, because the used PSF is a lower limit of the real one (see, for instance, Joshi et al. 2011). As a consequence, the continuum contrast has only changed from 6.3% in the original data to 11.8% in the deconvolved data. This value is clearly below the figure of 13–14% found in the simulations (Danilovic et al. 2008). Second, we checked that the original (nondeconvolved) Stokes *V* profiles of the 80% of those pixels that harbor an inverse polarity in the deconvolved map present the characteristic third lobe in the red wing of Stokes V in the original data (37% of the penumbral pixels harbor such a third lobe in the original data). Following Franz (2011), this is a hint of the presence of a hidden field with opposite polarity. With these two points we want to demonstrate that we are not introducing new information by the deconvolution
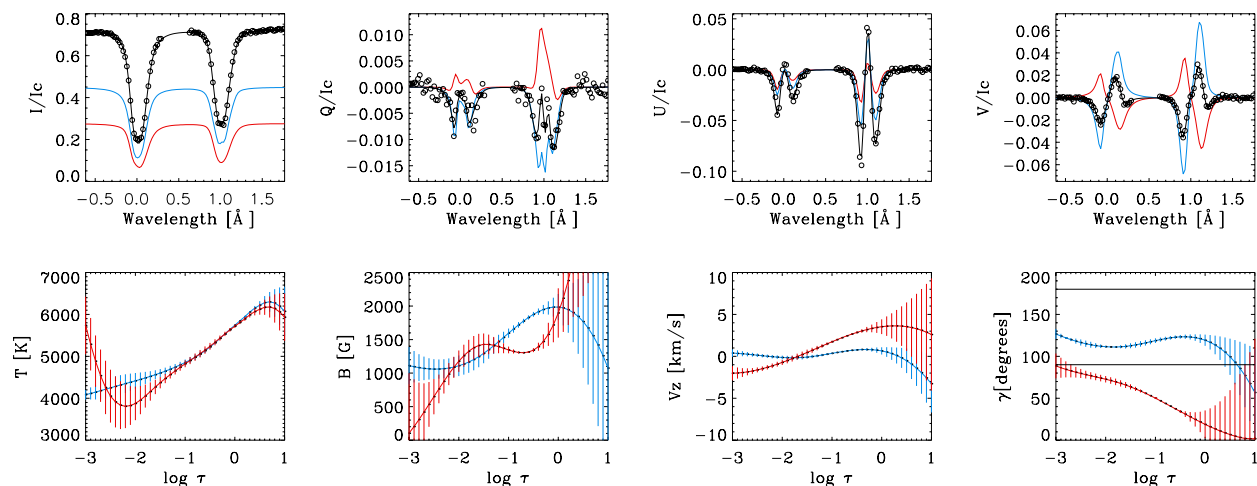
Fig. 5. *Upper 4 panels*: original (before deconvolution) Stokes profiles and best fits obtained by a 2-component SIR inversion applied to the inverse polarity pixel shown in Fig. 4. The two components are depicted in blue and red, and the combination in black line. *Lower 4 panels*: the two atmospheric models.

of the PSF. We are simply disentangling mixed information. As an illustration, we present in Fig. 5 the Stokes profiles before the deconvolution of the same inverse polarity profile that we plotted in Fig. 4. Note the presence of the third, inverse polarity, lobe at the red wing of the Stokes *V* profiles of both spectral lines. We inverted these original (nondeconvolved) Stokes profiles using SIR, but now considering a two-component atmosphere. In the lower panels one can see the corresponding optical depth stratification of the different quantities for both models. Interestingly, the model of the red component is quite similar to the corresponding model of the deconvolved profile shown in Fig. 4. The model of the blue component explains the contamination by stray light, and consequently it is similar to the model that reproduces a bright pixel. For this reason, the blue model is quite similar to the blue model presented in Fig. 4.

6. Conclusions

We report here observations of reversed polarity fields at the border of bright penumbral filaments in the whole penumbra. The spatial distribution of the reversed polarity fields is similar to what is predicted by the most recent numerical simulations (Rempel 2012). This has been possible after deconvolution of the original data using a regularization method based on a principal component decomposition of the profiles.

The Stokes profiles of those pixels that show a reversed polarity in the deconvolved map display a small opposite polarity third lobe on the red wind in the original data. This is a clear hint of hidden reversed polarity fields (Franz 2011). We found a reversed flux in the penumbra at optical depth $\tau = 0.1$ of 8.4% of the total unsigned penumbral flux. It corresponds to 17% of the pixels of the penumbra. Seventy-two percent of these pixels present positive velocity (downflow). All these facts indicate that we have found observational proof of convection in sunspot penumbra filaments.

References

Bellot Rubio, L. R. 2010, in Magnetic coupling between the Interior and the Atmosphere of the Sun, eds. S. S. Hassan, & R. J. Rutten, Ap&SS Proc., 193
Borrero, J. M. 2009, Sci. China Ser. G, 52, 1670
Borrero, J. M., & Ichimoto, K. 2011, Liv. Rev. Sol. Phys., 8, 4
Brault, J., & Neckel, H. 1987, Spectral Atlas of the Solar Absolute Disk-Averaged and Disk-Center Intensity from 3290 to 12 510 Å (unpublished, ditigal IDL version provided in the KIS sofware lib)
Danilovic, S., Gandorfer, A., Lagg, A., et al. 2008, A&A, 484, L17
del Toro Iniesta, J. C., Bellot Rubio, L. R., Collados, M. 2001, ApJ, 549, L139
Elmore, D. F., Lites, B. W., Tomczyk, S., et al. 1992, Proc. SPIE, 1746, 22
Franz, M. 2011, Ph.D. Thesis [arXiv:1107.2586]
Ichimoto, K. 2010 in Magnetic Coupling between the Interior and Atmosphere of the Sun, eds. S. S. Hasan, & R. J. Rutten, Ap&SS Proc., 186
Joshi, J., Pietarila, A., Hirzberger, J., et al. 2011, ApJ, 734, L18
Kosugi, T., Matsuzaki, K., Sokao, T., et al. 2007, Sol. Phys., 243, 3
Kurucz, R. L., Furenlid, I., Brault, J., & Testerman, L. 1984, Solar flux atlas from 296 to 1300 nm (National Solar Observatory, Sunspot, NM)
Langhans, S., Scharmer, G. B., Kiselman, D., Löfdahl, M. G., & Berger, T. E. 2005, A&A, 436, 1087
Lites, B. W., Elmore, D. F., & Streander, K. V. 2001, ASPC, 236, 33
Louis, R. E., Bellot Rubio, L. R., Mathew, Sh. K., & Venkatakrishnan, P. 2009, ApJ, 704, L29
Louis, R. E., Bellot Rubio, L. R., Mathew, Sh. K., & Venkatakrishnan, P. 2011, ApJ, 727, 49
Lucy, L. B. 1974, AJ, 79, 745
Rempel, M. 2012, ApJ, 750, 62
Rempel, M., Schüssler, M., Cameron, R.H., & Knölker, M. 2009a, Science, 325, 171
Rempel, M., Schuessler, M., & Knoelker, M. 2009b, ApJ, 691, 640
Richardson, W. H. 1972, J. Opt. Soc. Am. (1917-1983), 62, 55
Ruiz Cobo, B., & del Toro Iniesta, J. C. 1992, ApJ, 398, 375
Sánchez Almeida, J. 2005, ApJ, 622, 1292
Scharmer, G. B., & Henriques, V. M. J. 2012, A&A, 540, A19
Scharmer, G. B., Henriques, V. M. J., Kiselman, D., & de la Cruz Rodríguez, J. 2011, Science, 333, 316
Schlichenmaier, R. 2009, Space Sci. Rev., 144, 213
Socas-Navarro, H. 2011, A&A, 529, A37
Suematsu, Y., Tsuneta, S., Ichimoto, K., et al. 2008, Sol. Phys., 249, 197
Tritschler, A. 2009, in Proc. Second Hinode Science Meet., eds. M. Cheung et al., ASP Conf. Ser., 415, 339
van Noort, M. 2012, A&A, 548, A5
Westendorp Plaza, C., del Toro Iniesta, J. C., Ruiz Cobo, B., et al. 1997, Nature, 389, 47
Westendorp Plaza, C., del Toro Iniesta, J. C., Ruiz Cobo, B., et al. 2001, ApJ, 547, 1130